Research Article Vol. 33, No. 7 / 7 Apr 2025 / Optics Express 15888
Optics EXPRESS

High-spatial-frequency nanoripples induced on a WS_2 film by femtosecond laser pulses for second harmonic generation and Raman scattering manipulation

JINSHAN LUO,[1,†] SHULEI LI,[2,†] SHIMEI LIU,[1] YUHENG MAO,[1] ZHUO WANG,[1,3] AND SHENG LAN[1,4]

[1]Guangdong Provincial Key Laboratory of Nanophotonic Functional Materials and Devices, School of Optoelectronic Science and Engineering, South China Normal University, Guangzhou 510006, China
[2]School of Optoelectronic Engineering, Guangdong Polytechnic Normal University, Guangzhou 510665, China
[3]zhuowang@m.scnu.edu.cn
[4]slan@scnu.edu.cn
[†]These authors contributed equally.

Abstract: Transition metal dichalcogenides (TMDCs) have attracted great interest due to their unique layer-related electronic and optical properties, which exhibit potential applications in optoelectronic devices. However, the fabrication of nanostructures on the surface of a TMDC film, which is necessary for their device applications, remains a big challenge. Direct laser writing has been widely employed to fabricate periodic structures on the surface of metallic and dielectric materials. Here, we demonstrate that high-spatial-frequency nanoripples with a period of only one-tenth of the laser wavelength could be produced on the surface of a WS_2 film by using femtosecond laser ablation. The period of nanoripples is controlled by adjusting the WS_2 film thickness and laser fluence, and their orientation is perpendicular to the writing laser polarization. It is revealed that the fabricated nanoripples exhibit polarization control for reflected light, second harmonic wave, and Raman signal. Interestingly, the second harmonic generation is enhanced (suppressed) when the polarization of the excitation light is parallel (perpendicular) to the orientation of nanoripples. In addition, the Raman signals are greatly enhanced in the presence of nanoripples. Based on numerical simulation, it is unveiled that the modification in the electric field distribution in the WS_2 film induced by nanoripples plays a crucial role in the second harmonic generation. At the same time, Raman signals are enhanced by the compressive strain formed in nanoripples. Our findings indicate the potential applications of the high-spatial-frequency nanoripples in controlling the optical properties of the TMDCs and pave the way for realizing polarization-sensitive optical storage and display based on TMDCs.

1. Introduction

Transition metal dichalcogenides (TMDCs), such as tungsten sulfide (WS_2) [1,2] and molybdenum sulfide (MoS_2) [3], have emerged as promising materials for light-harvesting, photoluminescence, and optoelectronic applications due to their unique layer-dependent electronic and optical properties and large refractive indices. Single-layer TMDCs possess direct bandgaps and large exciton binding energies, making them ideal for achieving high-efficiency light emission and exploring strong exciton-photon/plasmon coupling. Research has shown that WS_2 and MoS_2 monolayers produce the most intense second harmonic generation (SHG), with SHG signal strength diminishing sharply as the number of layers increases. In bulk transition metal dichalcogenides (TMDCs), the SHG effect becomes nearly undetectable, as destructive interference between neighboring atomic layers cancels out the response, as demonstrated in

#555503 https://doi.org/10.1364/OE.555503
Journal © 2025 Received 13 Jan 2025; revised 16 Mar 2025; accepted 16 Mar 2025; published 1 Apr 2025

Optics EXPRESS

prior studies [4–6]. In addition, the crystal symmetry of multilayer TMDCs can be disrupted by introducing structural defects or applying local strain, significantly altering their nonlinear optical responses. So far, various strategies have been proposed to enhance the nonlinear optical responses of multilayer TMDCs, including defect engineering [7], strain engineering [8], controlled stacking sequences [9], and fabrication of nanowires and nanoparticles [10–12].

Recently, it has been revealed that nanoparticles made of TMDCs can support Mie resonances in the near-infrared spectral range because of their high refractive indices and low optical loss [13]. Efficient wavefront phase shaping can be realized with metalenses composed of nanodisk arrays made of high-refractive-index TMDCs [14]. Furthermore, precise control of photon-exciton strong coupling is achieved by exploiting the bound states in the continuum formed in a metasurface composed of WS_2 nanobricks [15]. Fabricating TMDC-based metasurfaces typically requires complex multistep processes, including chemical vapor deposition, electron-beam lithography, and reactive ion etching. In contrast, femtosecond laser ablation [16–19] enables direct fabrication of periodic nanostructures on diverse material surfaces, offering distinct advantages in cost efficiency, scalability, and processing speed. Importantly, laser-induced periodic surface structures with periods much smaller than the laser wavelength can be fabricated by using direct laser writing, providing a platform for studying the optical properties of deep-subwavelength nanostructures [20–22]. Moreover, it has been demonstrated that the van der Waals interaction between atomic layers and the significant temperature gradient induced by the laser can be exploited to realize laser exfoliation with an atomic-layer-precise for multilayer TMDCs [23].

The formation of laser-induced periodic structures on semiconductor surfaces is primarily driven by light interference phenomena, including interactions between incident light and scattered light [24], incident light and surface plasmons [25], and nonlinear harmonics and their scattered waves. Among these mechanisms, nonlinear harmonics with wavelengths smaller than the excitation light play a pivotal role in enabling high-spatial-frequency periodic structures, as their short wavelength enhances the resolution of finer patterns. For example, a TiO_2 layer formed on the surface of a Ti substrate has a strong third harmonic generation effect, which is crucial for the fabrication of high-spatial-frequency nanoripples under the irradiation of femtosecond laser pulses [26]. It should be emphasized that the modification in the optical properties of semiconductors induced by the high-density free electrons in the conduction band is also important for producing high-spatial-frequency periodic surface structures [27–29].

The nonlinear optical responses of multilayer TMDCs can be greatly modified by using metallic substrates [30–32]. As compared with a single-layer MoS_2 on a SiO_2/Si substrate, it has been shown that a multilayer MoS_2 on an Au/SiO_2 substrate exhibits significantly enhanced SHG because the electric field intensity in the multilayer MoS_2 is greatly improved in the presence of the Au film [33]. It implies that using an Au/SiO_2 substrate may facilitate the formation of high-frequency nanoripples in multilayer TMDCs due to significantly enhanced SHG. On the other hand, it is expected that the nonlinear optical responses of TMDCs can be modified by the deep-subwavelength nanostructures or high-spatial-frequency nanoripples induced on the surface of the TMDCs. For example, monolayer MoS_2 nanoripples with sub-20 nm widths have anisotropic light absorption, leading to strong polarization dependence of Raman spectra [34]. However, the nanoripples do not exhibit influence on the polarization dependence of SHG. In addition, laser ablation applied to TMDC materials can also effectively enhance photothermal conversion efficiency [35], diode rectification properties [36], and photoluminescence [37].

In this work, we investigate the deep-subwavelength nanoripples induced on the surface of a multilayer WS_2 film on an Al_2O_3/Au/SiO_2 substrate and the influence of such nanoripples on the optical properties of the WS_2 film. It is found that the writing laser energy density determines the morphology and period of the nanoripple formed on the WS_2 film. More interestingly, it is revealed that the nanoripples exhibit polarization control for the reflected light, second harmonic

Optics EXPRESS

wave, and Raman signal. These phenomena can be explained by the influences of periodic nanostructures and local strains introduced by the nanoripple on linear and nonlinear optical responses of the WS_2 film. Our findings indicate the potential applications of high-frequency nanoripples on the surface of a TMDC film in the fields of optical memory and nanoscale display.

2. Result and discussion

2.1. Formation of nanoripples on multilayer WS_2 films

Figure 1(a) schematically shows the laser writing process of nanoripples on a piece of multilayer WS_2 film placed on an $Al_2O_3/Au/SiO_2$ hybrid substrate. The morphology of nanoripples can be controlled by tuning the energy density of the incident laser. To systematically analyze this relationship, we introduced two parameters: the low-spatial-frequency period (P_l) and the high-spatial-frequency fringe period (P_h), which enable a detailed discussion across varying experimental conditions. The thickness of multilayer WS_2 films and the depth of induced nanoripples are represented by the parameters T and h, respectively. Detailed descriptions of the fabrication processes and measurement methodologies are provided in Section 3.

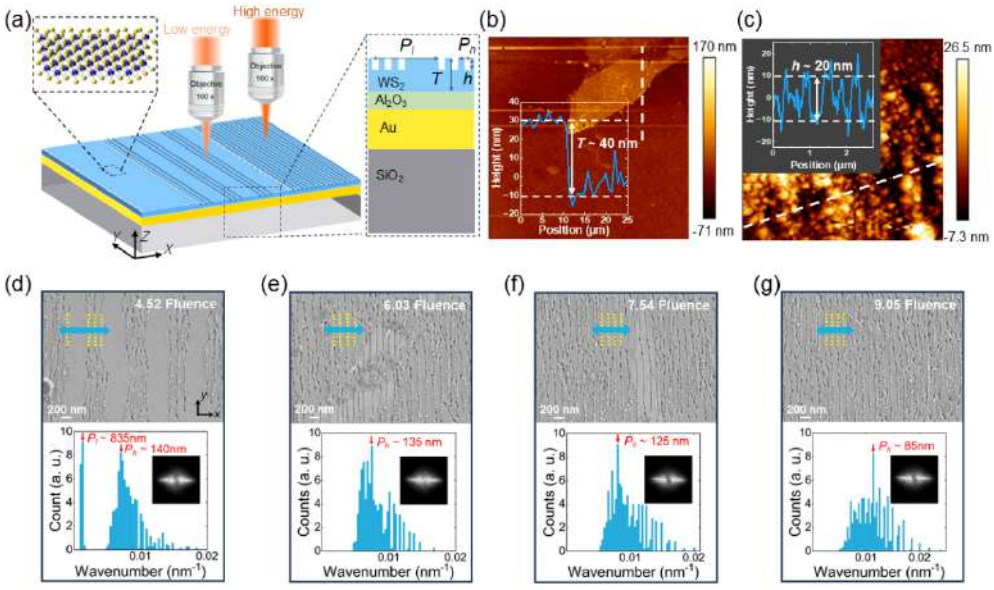

Fig. 1. (a) Schematic of writing process and structure of low- and high-spatial-frequency nanoripples on the surface of multilayer WS_2 placed on an $Al_2O_3/Au/SiO_2$ substrate by using focused femtosecond laser pulses at 800 nm. (b) The AFM image of the uniform multilayer WS_2 film, the height profile along the white dashed line is shown in the inset indicating a film thickness of $T \sim 40$ nm. (c) The AFM image of a typical high-spatial-frequency nanoripple, the height profile along the white dashed line is shown in the inset indicating a nanoripple depth of $h \sim 20$ nm. (d-e) The SEM images of nanoripples induced by laser irradiation at energy densities of 4.52, 6.03, 7.54, and 9.05 mJ/cm^2, respectively (upper panels). In each image, the yellow dashed line represents the orientation of the nanoripple, and the blue arrow indicates the writing laser polarization direction. The lower panels and insets show the corresponding Fourier transformation spectra and images, revealing the period and orientation of the nanoripples.

The target uniform multilayer WS_2 film is measured by atomic force microscopy (AFM), and the result is shown in Fig. 1(b). The inset indicates the height profile along the white dashed line. It is shown that the thickness of the multilayer WS_2 film is ~ 40 nm. Then the sample is

Optics EXPRESS

illuminated by focused 800 nm femtosecond laser pulses with a fluence of 7.54 mJ/cm^2. Next, the induced nanoripple is measured by AFM either. In Fig. 1(c), the inset shows the height profile along the white dashed line perpendicular to the nanoripple orientation. It shows that the nanoripples have an average depth of 20 nm. To determine the influence of laser energy density, laser pulses with different fluences are adopted to write nanoripples on the same sample. The corresponding scanning electron microscope (SEM) images and Fourier transformation of the SEM images are shown in Figs. 1(d)-(g). As shown by Fig. 1(d), when the writing laser fluence is relatively low ($F = 4.52$ mJ/cm^2), both low- and high-spatial-frequency nanoripples are formed on the multilayer WS_2. The orientation of the nanoripples is along the y direction, which is perpendicular to the polarization (blue arrow) of the writing laser pulses. The Fourier transformation spectrum indicates that the low- and high-spatial-frequency nanoripples periods are estimated to be $P_l \sim 835$ nm and $P_h \sim 140$ nm, respectively. When the laser fluence increases to 6.03 mJ/cm^2, the low-spatial-frequency nanoripple vanishes, and the period of the high-spatial-frequency nanoripple decreases to ~ 135 nm as shown in Figs. 1(e). With the further increase of the writing laser fluence, the period of the nanoripple will further decrease. It can be seen from Figs. 1(f) and (g) that under the condition of 7.54 mJ/cm^2 and 9.05 mJ/cm^2, the period of the formed nanoripples are ~ 125 nm and ~ 85 nm, respectively. It is revealed that the period of the laser-induced nanoripple can be effectively manipulated by tuning the laser fluence.

To examine the influence of WS_2 film thickness on the formation quality of the nanoripples, we repeat the nanoripple fabrication process using multilayer WS_2 films with thicknesses of ~ 20 nm and ~ 80 nm. Nanoripples cannot be induced on the ~ 20 nm WS_2 sample until the laser fluence increases to 10.55 mJ/cm^2. The SEM image in Fig. 2(a) shows that only high-spatial-frequency nanoripples are formed. The Fourier transformation spectrum of the SEM image shows that the main period of the nanoripples is ~ 140 nm. However, due to the thickness of the sample itself is low, the resulting nanoripple depth is limited, and the orientation of the fringe is poor. For the case of the multilayer WS_2 film with a thickness of ~ 80 nm, both low- and high-spatial-frequency nanoripples can be produced simultaneously even at a very high writing laser fluence. In the experiment, due to the upper limit of the power that the lens can withstand, the maximum laser fluence we adopted is 12.06 mJ/cm^2, and the induced nanoripple structure is shown in Fig. 2(b). According to the Fourier transformation spectrum, the periods of the low- and high-frequency components are 500 nm and 130 nm, respectively. The above results show that the period and regularity of laser-induced nanoripples are susceptible to the thickness of the sample. Similar laser-induced periodic structures dependent on the thickness of the target film have also been reported in metal samples [38].

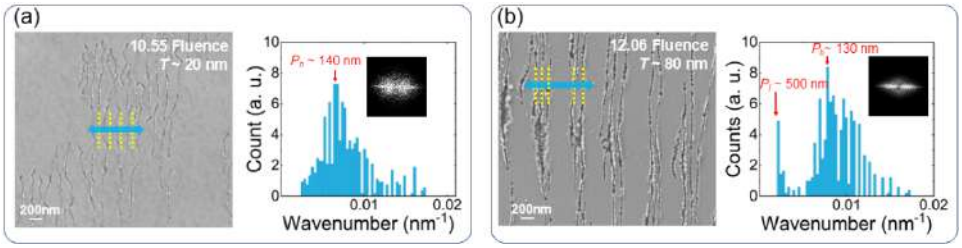

Fig. 2. (a) The SEM image and the corresponding Fourier transformation spectrum and image of the nanoripple form on a multilayer WS_2 film with a thickness of $T \sim 20$ nm. (b) The SEM image and the corresponding Fourier transformation spectrum and image of the nanoripple form on a multilayer WS_2 film with a thickness of $T \sim 80$ nm. In each image, the yellow dashed line represents the orientation of the nanoripple, and the blue arrow indicates the writing laser polarization orientation.

Optics EXPRESS

2.2. Polarization control of reflected light

It is expected that the nanoripple formed on the WS_2 film will exhibit polarization-dependent reflection [39]. We chose nanoripples fabricated under the laser fluence of 9.05 mJ/cm^2 as the target sample. The reflectivity spectra of the sample illuminated by white light with different polarization orientations are shown in Fig. 3(a). For comparison, the polarization-dependent reflectivity spectra measured for the corresponding uniform multilayer WS_2 film are shown in Fig. 3(d). In both cases, one can identify two reflection dips appearing at ~ 622 and ~ 515 nm, which originate from the optical absorption caused by the A- and B-excitons in the WS_2 film, respectively [40,41]. For the uniform WS_2 film, only a small difference is observed between the reflectivity spectra measured at 0° and that measured at 90°. From the bright-field images shown by the insets of Fig. 3(d), the color of the uniform WS_2 film appears a bit brighter under 90° polarized-light illumination than under 0° polarized-light illumination. It arises mainly from the difference in optical absorption affected by crystal direction. In contrast, the WS_2 nanoripples exhibit much lower reflectivity for the light polarized perpendicular to the nanoripple (polarization angle is 0°). Additionally, a significant reduction of reflectivity within the wavelength range from 450 to 750 nm is observed for *x*-polarized light (0°) compared to *y*-polarized light (90°) as shown in Fig. 3(a). For incident light polarized perpendicular to the nanoripples, the lossy gap mode supported by the nanoripples reduces reflectivity [42]. Because the lossy gap mode has a certain spectral width, the attenuation in the center of the spectrum is greater than the attenuation in the sideband. Conversely, when the incident light is polarized parallel to the nanoripples, weak coupling with the lossy gap mode results in only slight, uniform attenuation across the spectrum. The "letter A" patterns in the insets further demonstrate a remarkable contrast in reflectivity between the two polarization states. These observations confirm that laser-induced nanoripples can achieve polarization-dependent reflectivity.

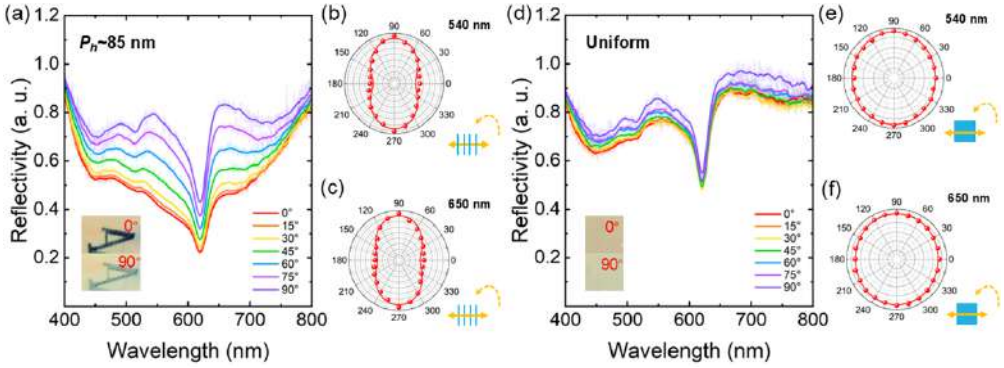

Fig. 3. Polarization-dependent reflectivity of the nanoripple. (a) Reflectivity spectra of the WS_2 nanoripple under illumination with white light at different polarization angles. The insets are bright-field images of the sample. The polarization characteristic of the WS_2 nanoripple at the wavelengths of (b) 540 nm, and (c) 650 nm are measured with the polarization angle varying from 0°to 360°. The inset shows the polarization (yellow arrow) of the probe light and the orientation of the nanoripple (blue lines). (d) Reflectivity spectra of the uniform WS_2 film under illumination with white light at different polarization angles. The polarization characteristic of the uniform WS_2 film at the wavelengths of (e) 540 nm, and (f) 650 nm are measured with the polarization angle varying from 0°to 360°.

To provide a more detailed analysis of the nanoripple-caused anisotropic reflectivity, we collect the reflectivity data of light with polarization from 0° to 360° in steps of 15° at the two representative wavelengths (540 nm and 650 nm), and display them using polar coordinate maps, as shown in Figs. 3(b) and (c). As the polarization direction (yellow arrow) of the incident

Optics EXPRESS

light is rotated 360° anticlockwise, the measured reflectivity fluctuates significantly, showing an obvious elliptical trajectory in polar coordinates. The long and short axes of the elliptic trajectory are parallel and perpendicular to the orientation direction of the nanoripple, respectively. For the corresponding results of the uniform WS_2 film presented in Figs. 3(e) and 3(f), the reflectivity does not exhibit obvious dependence on the polarization of the illumination light. These results indicate the potential applications of the nanoripples fabricated by direct laser writing in polarization-sensitive optical display technique.

2.3. Polarization control of SHG

Using direct laser writing technique at the wavelength of 800 nm, we made two nanoripple patterns, a "letter A" and a "flower", on the WS_2 film ($T \sim 40$ nm) with a period of $P_h \sim 79$ nm and ~ 85 nm, respectively. The bright-field image of the WS_2 film after patterning is shown in Fig. 4(a). Then, we mapped the SHG intensity of the WS_2 film by using a two-photon laser scanning confocal microscope. A 60× objective lens (NA = 0.85) is used to focus 800 nm femtosecond laser light with a much lower energy density (~ 0.85 mJ/cm^2) on the WS_2 film. The scanning images of SHG obtained by using y- and x-polarized femtosecond laser light are shown in Figs. 4(b) and 4(c), respectively. Interestingly, it is found that the SHG intensity on the nanoripple is enhanced for the y-polarized light and reduced for the x-polarized light when compared with the result of the uniform WS_2 film. The enhancement or reduction factor is defined as the SHG intensity of the patterned region divided by the SHG intensity of the uniform WS_2 film region. For the x-polarized light, we observed SHG enhancement factors of ~ 3.63 and ~ 2.44 in the regions of "letter A" and "flower", respectively. Conversely, for the y-polarized light, the SHG intensities in the "letter A" and "flower" are suppressed with reduction factors of ~ 0.54 and ~ 0.32 as compared with that of the uniform WS_2 film.

To gain a deep insight into the modification in SHG intensity induced by the nanoripple, we examined the dependence of the SHG intensity on the polarization angle of the excitation light observed in the nanoripples with different periods (from 90 to 80 nm), as shown in Figs. 4(d) -(f). For the WS_2 film with nanoripples, the SHG intensity increases continuously when the polarization angle is increased from 0° to 90°. The maximum intensity observed at $\theta = 90°$ is about 4.7 times larger than the minimum intensity observed at $\theta = 0°$ as illustrated in Fig. 4(d). This feature differs from the sixfold rotational symmetry of the SHG intensity of uniform WS_2 films reported in the literature [43,44]. It implies that the original polarization-dependent SHG in a WS_2 film, which is governed by the crystal structure, can be modified by the nanoripples induced in the WS_2 film. In addition, as shown by Figs. 4(e) and 4(f), the strongest second harmonic intensity produced by the samples is 10.7, and 12.3 times that of the respective weakest case, respectively. It is found that a smaller nanoripple period leads to a larger intensity difference between the SHG intensity excited by the x- and y-polarized laser light. It implies that nanoripples with a higher spatial frequency exhibit a stronger ability in modulating SHG intensity.

To reveal the physical mechanism behind the experimental observation, we simplified the nanoripple as a nanograting and used the finite-difference time-domain (FDTD) method based on Lumerical to simulate the near-field distribution in the nanoripple excited by a normally incident plane wave with different polarization directions. The parameters of the nanoripple are $P_h = 85$ nm, $W = 15$ nm, $h = 20$ nm, and $T = 40$ nm. Figure 4(g) shows the calculated field distribution of E_x when the nanoripple is excited by an x-polarized plane wave with normal incidence. It is found that the excited mode is the combination of the air gap mode in the WS_2 nanoripple and the surface plasmon polariton (SPP) at the Au/SiO_2 interface. Therefore, the phase of E_x varies periodically in the direction perpendicular to the nanoripple orientation. As the phase of SHG is determined by the phase of excitation light, in Fig. 4(g), second harmonic waves generated in adjacent regions with opposite phases of electric fields will have destructive interference. Consequently, although x-polarized excitation light can produce significant near-field enhancement, the corresponding

Optics EXPRESS

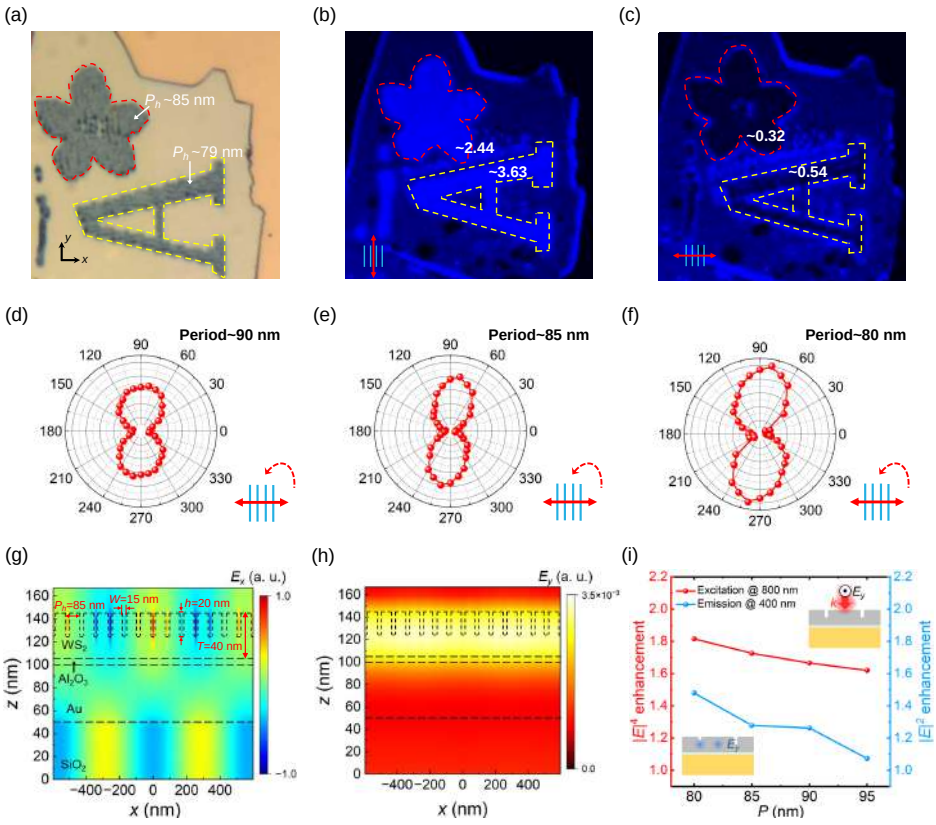

Fig. 4. Polarization-dependent second harmonic waves produced by the uniform WS_2 film and the nanoripple. (a) Bright-field image of nanoripple patterns fabricated on a WS_2 film. The periods of the nanoripples in the regions of "flower" and "letter A" are ~ 85 nm and ~ 79 nm, respectively. (b) and (c) show SHG scanning images excited by low-fluence femtosecond laser pulses at the wavelength of 800 nm, where *y*-polarized and *x*-polarized light are used, respectively. The red arrow and blue lines show the polarization of the scanning laser and the orientation of nanoripples, respectively. The SHG enhancement and reduction factors of nanoripples compared to the uniform WS_2 film are also displayed in the figures. (d)-(f) show the polarization-dependent amplitude of the second harmonic wave in the nanoripples with different periods. The polarization angle of the incident laser is changed in steps of 10°. (g) Simulated E_x distribution in the *x*-*z* plane excited by an *x*-polarized (perpendicular to the nanoripple) plane wave at 800 nm. (h) Simulated E_y distribution in the *x*-*z* plane excited by a *y*-polarized (parallel to the nanoripple) plane wave at 800 nm. (i) The enhancement factors of *y*-polarized light at excitation (800 nm) and emission (400 nm) wavelengths produced by the nanoripple.

Optics EXPRESS

SHG in the WS_2 nanoripple is suppressed due to destructive interference, which is the main difference from the previous work [42]. For the case of *y*-polarized light excitation, the $|E|^4$ in the nanoripple is larger than that in the uniform WS_2 film, meanwhile, the phase of local field in the WS_2 nanoripple is nearly uniform as shown in Fig. 4(h), therefore the SHG will be enhanced instead of suffering destructive interference. According to nonlinear optical theory, the intensity of SHG is proportional to the square of the pump light intensity [45]. Thus, the enhancement of SHG can be quantitatively evaluated using the enhancement factor of $|E|^4$ for the excitation light. In Fig. 4(i), under the excitation of a *y*-polarized plane wave, the enhancement factor of $|E|^4$ in the WS_2 nanoripple compared with that in a uniform WS_2 film is shown by red dots. It is found that, when other parameters are constant, the enhancement factor at the excitation wavelength increases with the decrease of the structure period. Besides, the nanoripples can also enhance the radiation intensity of the second harmonic wave. We calculated the out-of-plane radiation enhancement factor of two *y*-polarized electric dipoles placed in the WS_2 nanoripple. The two dipoles are placed at the position where the excitation electric field is enhanced most. To average out the effects of different areas of the nanoripple, the left dipole is placed at the groove and the right dipole is placed between the two grooves. A receiving plane is set above the nanoripple. The total radiation intensity can be obtained by integrating $|E|^2$ in the receiving plane. The ratio of the integrated $|E|^2$ for nanoripples to that for the uniform WS_2 film is defined as out-of-plane emission enhancement factor. In Fig. 4(i), the blue dots show that the enhancement factor of emission intensity at 400 nm grows with the reduction of the structure period. Moreover, after multiplying the excitation enhancement factor with the emission enhancement factor, the calculated SHG enhancement factors are ~ 2.7 and ~ 2.2 when $P_h = 80$ nm and 85 nm, respectively. The results are close to the experimental values of ~ 3.63 ("letter A" region with P_h ~ 79 nm) and ~ 2.44 ("flower" region with P_h ~ 85 nm). Another factor that affects the strength of SHG is the structural defects and local strains in the WS_2 nanoripple [46,47]. For the laser light polarized along the nanoripple orientation, the grooves act as structure defects, reducing the symmetry in the crystal structure, and leading to further enhancement in SHG. Therefore, measured enhancement factors are slightly higher than the values obtained by simulation. The strain properties in the nanoripple can be obtained by Raman spectroscopy, which will be discussed in the next section.

2.4. Polarization control of Raman signals

Raman spectroscopy is an important optical tool for material characterization. We examined the influence of nanoripples with a period of ~ 85 nm on the Raman response of WS_2 samples. The Raman scanning images of the $\mathbf{E}^1_{2g}$ mode of WS_2 (350 cm^{-1}) obtained by using laser light with polarization directions parallel and perpendicular to the orientation of the nanoripple are shown in Figs. 5(a) and 5(b), respectively. In both cases, the regions decorated with nanoripples are enclosed by dashed curves. The orientation of the nanoripples (blue lines) and the polarization (red arrow) of the laser light are shown in the insets. The formation of nanoripple leads to the enhancement in the Raman signals ($\mathbf{E}^1_{2g}$ mode) of WS_2. It is noticed that a larger enhancement factor is achieved when the laser light is polarized along the *y* direction (parallel to the nanoripple). In Figs. 5(c) and 5(d), we compare the Raman spectra obtained in the regions with and without nanoripples by using an excitation laser with different polarizations. The weak Raman signals (blue curves) detected from the uniform WS_2 film in Figs. 5(c) and 5(d) are magnified by ~ 64 and ~ 3 times, respectively, to facilitate direct comparison with the red curve data. Through directly dividing the Raman signal on the WS_2 nanoripples by that on the uniform WS_2 film, one can obtain an enhancement factor of ~ 64 at the $\mathbf{A}_{1g}$ and $\mathbf{E}^1_{2g}$ modes when the polarization of the excitation laser is parallel to nanoripples. In comparison, a much smaller enhancement factor (~ 3) is observed when the polarization of the laser is perpendicular to the nanoripple. In addition, the spectral broadening around the peak of $\mathbf{E}^1_{2g}$ mode shown in Fig. 5(c) can be attributed to the

Optics EXPRESS

emergence of new Raman modes caused by singularities in the vibrational density of states at nanoripple edges [34].

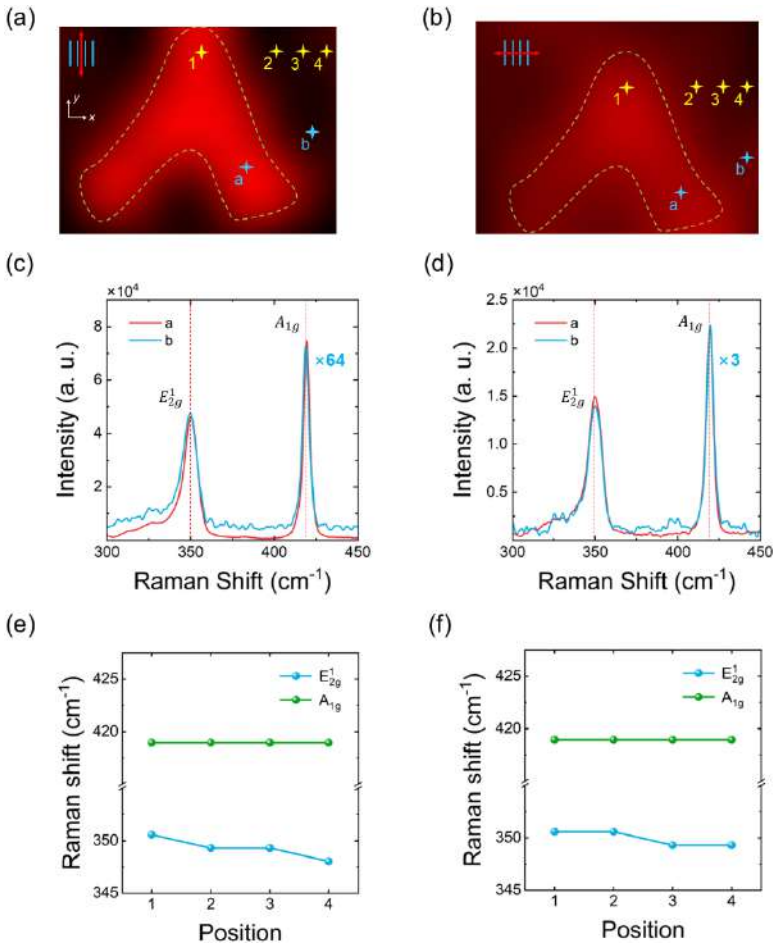

Fig. 5. Polarization-dependent Raman signals of the nanoripple with a period of ~ 85 nm. (a) Raman scanning image of the WS_2 nanoripple at 350 cm^{-1} ($\mathbf{E^1_{2g}}$ mode) with *y*-polarized laser excitation. The blue lines indicate the orientation of the nanoripple, and the red arrow indicates the polarization direction of the scanning laser. (b) Raman scanning image of a WS_2 nanoripple at $\mathbf{E^1_{2g}}$ mode with *x*-polarized laser excitation. (c) and (d) show the Raman spectra of the nanoripple (at point a) and the WS_2 thin film (at point b) under *y*- and *x*-polarized excitation, respectively. The blue curves in (c) and (d) are magnified by factors of 64 and 3, respectively, to facilitate direct comparison with the red curve data. (e) and (f) show the Raman shift extracted from four different locations (points 1, 2, 3, and 4) in (a) and (b), respectively.

In general, the formation of nanoripples in a WS_2 film is usually accompanied by the introduction of strain in the WS_2 film. Physically, the strain introduced in the WS_2 film can be revealed by Raman signal measurement. In Raman scattering spectroscopy, the peak of $\mathbf{E^1_{2g}}$ represent in-plane vibrational mode and the peak of $\mathbf{A_{1g}}$ comes from the mode of out-of-plane vibration. Prior studies indicate that applying biaxial strain to a two-dimensional TMDC material causes simultaneous shifts in both the $\mathbf{E^1_{2g}}$ and $\mathbf{A_{1g}}$ modes [48]. However, when the applied strain is uniaxial, only the $\mathbf{E^1_{2g}}$ mode shifts and the position of $\mathbf{A_{1g}}$ mode remains unchanged

Optics EXPRESS

[49,50]. Here, we measured the Raman shift of $\mathbf{E}^1_{2g}$ and $\mathbf{A}_{1g}$ modes at different locations of the WS_2 sample by using laser light with polarization directions parallel and perpendicular to the nanoripples, as shown in Figs. 5(e) and 5(f). In both cases, no shift is observed for the $\mathbf{A}_{1g}$ mode. In contrast, one can identify a shift in the $\mathbf{E}^1_{2g}$ mode no matter whether the laser polarization is parallel or perpendicular to the nanoripples. A blue shift of 2.55 cm^{-1} is observed when the laser polarization is parallel to the nanoripples. In comparison, a smaller blue shift of 1.27 cm^{-1} is found for the laser polarization perpendicular to the nanoripples. Based on the results of existing works, compressive strain usually causes a blue shift of the $\mathbf{E}^1_{2g}$ peak [48] while tensile strain produces a red shift of the $\mathbf{E}^1_{2g}$ peak [49]. Therefore, it indicates that the uniaxial compressive strain is dominant in the target sample. In addition, the extent of the spectral shift further demonstrates that compressive strain impacts *y*-polarized light (oriented parallel to the nanoripple) more significantly than *x*-polarized light (oriented perpendicular to the nanoripple). Given that compressive strain is known to amplify the Raman signal effectively [48], this phenomenon explains the substantially greater Raman enhancement factor observed for *y*-polarized light compared to *x*-polarized light.

3. Methods

3.1. Fabrication procedure

The WS_2/Al_2O_3/Au heterostructure is prepared by the following three steps. First, an Au film with a thickness of ~ 50 nm is deposited on the SiO_2 substrate by electron beam evaporation technique. Then, an Al_2O_3 spacer with a thickness of ~ 5 nm is deposited on the Au film by using atomic layer deposition technology, the spacer can avoid contact between the top multilayer WS_2 and the Au film to reduce the quenching effect [51]. After that, a piece of multilayer WS_2 attached to polydimethylsiloxane (PDMS) is transferred onto the spacer to form a WS_2/Al_2O_3/Au heterostructure by imprinting the PDMS on the Al_2O_3/Au/SiO_2 substrate and heating at 120 °C for 10 minutes.

For the fabrication of WS_2 nanoripples, an 800 nm femtosecond laser beam with a repetition rate of 76 MHz and a duration of 130 fs is introduced into an inverted microscope (Axio Observer A1, Zeiss) and focused on the sample through a 100× objective lens (NA = 0.7). A three-dimensional positioning system driven by piezoelectric ceramics (P-563.3CD, Physik Instruments) with a step accuracy of 1 nm enables precise control of the laser illumination position. The laser spot moves in the same direction on the sample with a speed and step size of 1 μm/ms and 0.5 μm, respectively. A mechanical shutter is used for controlling the irradiation time of the laser, and the shutter opening time is set to 1 μs in the experiment.

3.2. Measurement setups

The height profile of the target WS_2 sample is measured by AFM (Nano Wizard 4 Nanoscience, JPK Instruments AG). The scanning step sizes for the uniform WS_2 film and the nanoripple are set to 0.3 μm and 0.1 μm, respectively. For the reflectivity measurement, a halogen lamp is used as a white light source, an objective lens is used for the collection of reflected light and the reflectivity spectra and sample images are measured by a spectrometer (SR-500i-B1, Andor) and a charge-coupled device (DU970 N, Andor), respectively. For the stimulation of nonlinear signals, the polarization of the incident laser is continuously tuned by an electrically driven λ/2 slide. The resulting second harmonic signal is collected by using the same objective lens and imported into the spectrometer on the microscope for analysis. A 60× objective lens (NA = 0.85) of a two-photon laser scanning confocal microscope (A1MP, Nikon) is used to focus the excitation laser and collect the stimulated second harmonic signal to obtain a scanning image. A 633 nm laser is introduced into a Raman scanning microscope to measure the Raman signal scanning image of the nanoripple and the Raman spectrum of the specific position on the target sample.

Optics EXPRESS

4. Conclusion

We have demonstrated that femtosecond laser interaction with multilayer WS_2 can induce the formation of deep-subwavelength period nanoripples on the surface. These nanoripples hold significant potential for high-quality optical data storage and polarization control. The orientation of the nanoripples is perpendicular to the polarization direction of the incident writing laser, while their period is tunable through adjustments in laser energy. Such deep-subwavelength nanoripples exhibit excellent modulation properties for reflectivity spectra, second harmonic intensity, and Raman signals. Firstly, as the polarization of incident light shifts from perpendicular (x-polarized) to the orientation of nanoripples to parallel (y-polarized), the reflectivity consistently rises within the visible wavelength range. Secondly, although *x*-polarized light can achieve higher near-field enhancement in the WS_2 nanoripples, the phase of its near field is periodically distributed in the *x* direction at 800 nm. Consequently, the corresponding SHG is suppressed due to the destructive interference between adjacent light with the opposite phase. On the other hand, destructive interference does not exist in the case of *y*-polarized excitation. In contrast, *y*-polarized light is enhanced by nanoripples at both excitation and emission wavelengths. In the meantime, the structural defects and local strain generated by the nanoripple can also contribute to the enhancement of SHG. Thus, an SHG enhancement of up to ~ 3.63 times is observed under *y*-polarized excitation. Thirdly, the anisotropic compressive strain is dominant in the nanoripple and a ~ 64-fold Raman signal enhancement is obtained for the *y*-polarized excitation. The results show that the nanoripples formed on multilayer WS_2 have a good application prospect in new photonic devices to realize polarization-sensitive nonlinear light emission, optical displays, and optical storage technology.

Funding. National Natural Science Foundation of China (12174123, 12374347); Natural Science Foundation of Guangdong Province (2022A1515010747).

Disclosures. The authors declare no conflicts of interest.

Data availability. Data underlying the results presented in this paper are not publicly available at this time but may be obtained from the authors upon reasonable request.

References

1. P. K. Barman, P. V. Sarma, M. M. Shaijumon, *et al.*, "High degree of circular polarization in WS_2 spiral nanostructures induced by broken symmetry," Sci. Rep. **9**(1), 2784 (2019).
2. H. Zhang, B. Abhiraman, Q. Zhang, *et al.*, "Hybrid exciton-plasmon-polaritons in van der Waals semiconductor gratings," Nat. Commun. **11**(1), 3552 (2020).
3. A. Splendiani, L. Sun, Y. B. Zhang, *et al.*, "Emerging Photoluminescence in Monolayer MoS_2," Nano Lett. **10**(4), 1271–1275 (2010).
4. J. Shi, P. Yu, F. Liu, *et al.*, "3R MoS_2 with broken inversion symmetry: a promising ultrathin nonlinear optical device," Adv. Mater. **29**(30), 1701486 (2017).
5. Y. Li, Y. Rao, K. F. Mak, *et al.*, "Probing symmetry properties of few-layer MoS_2 and h-BN by optical second-harmonic generation," Nano Lett. **13**(7), 3329–3333 (2013).
6. X. Lin, Y. Liu, K. Wang, *et al.*, "Two-dimensional pyramid-like WS_2 layered structures for highly efficient edge second-harmonic generation," ACS Nano **12**(1), 689–696 (2018).
7. H. G. Rosa, L. Junpeng, L. C. Gomes, *et al.*, "Second-harmonic spectroscopy for defects engineering monitoring in transition metal dichalcogenides," Adv. Opt. Mater. **6**(5), 1701327 (2018).
8. C. He, R. Wu, L. Zhu, *et al.*, "Anisotropic second-harmonic generation induced by reduction of in-plane symmetry in 2D materials with strain engineering," J. Chem. Phys. **13**(1), 352–361 (2022).
9. X. Fan, Y. Jiang, X. Zhuang, *et al.*, "Broken symmetry induced strong nonlinear optical effects in spiral WS_2 nanosheets," ACS Nano **11**(5), 4892–4898 (2017).
10. T. Yu, M. Panmai, S. Li, *et al.*, "Anisotropically enhanced second harmonic generation in a WS_2 nanoparticle driven by optical resonances," ACS Appl. Nano Mater. **7**(1), 726–735 (2024).
11. Q. Qian, R. Zu, Q. Ji, *et al.*, "Chirality-dependent second harmonic generation of MoS_2 nanoscroll with enhanced efficiency," ACS Nano **14**(10), 13333–13342 (2020).
12. M. Panmai, J. Xiang, L. Zhou, *et al.*, "Revealing Mie resonances with enhanced and suppressed second-order nonlinear optical responses in a hexagonal-prism-like MoS_2 nanoparticle," Laser Photonics Rev. **17**(11), 2300346 (2023).
13. R. Verre, D. G. Baranov, B. Munkhbat, *et al.*, "Transition metal dichalcogenide nanodisks as high-index dielectric Mie nanoresonators," Nat. Nanotechnol. **14**(7), 679–683 (2019).

Optics EXPRESS

14. C.-H. Liu, J. Zheng, S. Colburn, *et al.*, "Ultrathin van der Waals Metalenses," Nano Lett. **18**(11), 6961–6966 (2018).
15. T. Weber, L. Kühner, L. Sortino, *et al.*, "Intrinsic strong light-matter coupling with self-hybridized bound states in the continuum in van der Waals metasurfaces," Nat. Mater. **22**(8), 970–976 (2023).
16. S. Amoruso, A. Andreone, A. Bellucci, *et al.*, "All-carbon THz components based on laser-treated diamond," Carbon **163**, 197–201 (2020).
17. A. S. Roberts, S. M. Noyikov, Y. Q. Yang, *et al.*, "Laser writing of bright colors on near-percolation plasmonic reflector arrays," ACS Nano **13**(1), 71–77 (2019).
18. S. N. Chowdhury, P. Nyga, Z. A. Kudyshev, *et al.*, "Lithography-free plasmonic color printing with femtosecond laser on semicontinuous silver films," ACS Photonics **8**(2), 521–530 (2021).
19. C. Y. Zhang, J. W. Yao, C. Q. Li, *et al.*, "Asymmetric femtosecond laser ablation of silicon surface governed by the evolution of surface nanostructures," Opt. Express **21**(4), 4439–4446 (2013).
20. C. Y. Zhang, J. W. Yao, H. Y. Liu, *et al.*, "Colorizing silicon surface with regular nanohole arrays induced by femtosecond laser pulses," Opt. Lett. **37**(6), 1106–1108 (2012).
21. H. Li, C.-Y. Zhang, X.-F. Li, *et al.*, "Enhanced upconversion luminescence from ZnO/Zn hybrid nanostructures induced on a Zn foil by femtosecond laser ablation," Opt. Express **23**(23), 30118–30126 (2015).
22. J. W. Yao, C. Y. Zhang, H. Y. Liu, *et al.*, "Selective appearance of several laser-induced periodic surface structure patterns on a metal surface using structural colors produced by femtosecond laser pulses," Appl. Surf. Sci. **258**(19), 7625–7632 (2012).
23. D. Hu, H. Li, Y. Zhu, *et al.*, "Ultra-sensitive nanometric flat laser prints for binocular stereoscopic image," Nat. Commun. **12**(1), 1154 (2021).
24. R. Le Harzic, D. Dörr, D. Sauer, *et al.*, "Formation of periodic nanoripples on silicon and germanium induced by femtosecond laser pulses," Phys. Procedia **12**, 29–36 (2011).
25. J. Zhang, Y. He, B. Lam, *et al.*, "Real-time *in situ* study of femtosecond-laser-induced periodic structures on metals by linear and nonlinear optics," Opt. Express **25**(17), 20323–20331 (2017).
26. X.-F. Li, C.-Y. Zhang, H. Li, *et al.*, "Formation of 100-nm periodic structures on a titanium surface by exploiting the oxidation and third harmonic generation induced by femtosecond laser pulses," Opt. Express **22**(23), 28086–28099 (2014).
27. S. Höhm, M. Rohloff, A. Rosenfeld, *et al.*, "Dynamics of the formation of laser-induced periodic surface structures on dielectrics and semiconductors upon femtosecond laser pulse irradiation sequences," Appl. Phys. A **110**(3), 553–557 (2013).
28. J. Bonse, A. Rosenfeld, and J. Krüger, "Implications of transient changes of optical and surface properties of solids during femtosecond laser pulse irradiation to the formation of laser-induced periodic surface structures," Appl. Surf. Sci. **257**(12), 5420–5423 (2011).
29. E. V. Golosov, A. A. Ionin, Y. R. Kolobov, *et al.*, "Ultrafast changes in the optical properties of a titanium surface and femtosecond laser writing of one-dimensional quasi-periodic nanogratings of its relief," J. Exp. and Theor. Phys. **113**(1), 14–26 (2011).
30. J. Zeng, J. Li, H. Li, *et al.*, "Effects of substrates on the nonlinear optical responses of two-dimensional materials," Opt. Express **23**(25), 31817 (2015).
31. A. T. Nguyen, S. Kwon, J. Song, *et al.*, "Self-hybridized exciton-polaritons in sub-10-nm-thick WS_2 flakes: roles of optical phase shifts at WS_2/Au interfaces," Nanomaterials **12**(14), 2388 (2022).
32. E. Cho, A. T. Nguyen, S. Lim, *et al.*, "Thickness-dependent optical characteristics of WS_2 flakes prepared by Au- and Ag-assisted exfoliation," J. Phys. D: Appl. Phys. **56**(32), 325101 (2023).
33. J. Zeng, M. Yuan, W. Yuan, *et al.*, "Enhanced second harmonic generation of MoS_2 layers on a thin gold film," Nanoscale **7**(32), 13547–13553 (2015).
34. J.-B. Wu, H. Zhao, Y. Li, *et al.*, "Monolayer molybdenum disulfide nanoribbons with high optical anisotropy," Adv. Opt. Mater. **4**(5), 756–762 (2016).
35. F. Ullah, D. Chung, F. Ye, *et al.*, "Femtosecond laser carburization of WS_2 flakes to W_2C for enhanced photothermal conversion efficiency," Adv. Eng. Mater. **26**(12), 2302222 (2024).
36. K. Wang, Z. Chen, X. Wu, *et al.*, "Ultrafast mechanism of material removal in the femtosecond laser ablation of WS_2 and its diode rectification characteristics," Crystals **13**(5), 832 (2023).
37. C.-B. Qin, X.-L. Liang, S.-P. Han, *et al.*, "Giant enhancement of photoluminescence emission in monolayer WS_2 by femtosecond laser irradiation," Front. Phys. **16**(1), 12501 (2021).
38. H. Xie, B. Zhao, J. Cheng, *et al.*, "Super-regular femtosecond laser nanolithography based on dual-interface plasmons coupling," Nanophotonics **10**(15), 3831–3842 (2021).
39. S. Li, M. Panmai, S. Tie, *et al.*, "Regulating disordered plasmonic nanoparticles into polarization sensitive metasurfaces," Nanophotonics **10**(5), 1553–1563 (2021).
40. Y. Li, A. Chernikov, X. Zhang, *et al.*, "Measurement of the optical dielectric function of monolayer transition-metal dichalcogenides: MoS_2, $MoSe_2$, WS_2, and WSe_2," Phys. Rev. B **90**(20), 205422 (2014).
41. S. Li, L. Zhou, F. Deng, *et al.*, "Transverse-electric-polarized polaritons propagating in a WS_2/Si_3N_4/Ag heterostructure," Laser Photonics Rev. **16**(12), 2100457 (2022).
42. J. Shi, W. Y. Liang, S. S. Raja, *et al.*, "Plasmonic enhancement and manipulation of optical nonlinearity in monolayer tungsten disulfide," Laser Photonics Rev. **12**(10), 1800188 (2018).

Optics EXPRESS

43. C. Janisch, Y. Wang, D. Ma, *et al.*, "Extraordinary second harmonic generation in tungsten disulfide monolayers," Sci. Rep. **4**(1), 5530 (2014).
44. W. T. Hsu, Z. A. Zhao, L. J. Li, *et al.*, "Second harmonic generation from artificially stacked transition metal dichalcogenide twisted bilayers," ACS Nano **8**(3), 2951–2958 (2014).
45. N. Bernhardt, K. Koshelev, S. J. U. White, *et al.*, "Quasi-BIC resonant enhancement of second-harmonic generation in WS_2 monolayers," Nano Lett. **20**(7), 5309–5314 (2020).
46. A. Dewambrechies, A. Y. Polyakov, B. Küçüköz, *et al.*, "Enhanced second-order nonlinearities at strained ultrasharp zigzag edges in multilayer MoS_2," J. Phys. Chem. C **127**(31), 15395–15405 (2023).
47. L. Mennel, M. Paur, and T. Mueller, "Second harmonic generation in strained transition metal dichalcogenide monolayers: MoS_2, $MoSe_2$, WS_2, and WSe_2," APL Photonics **4**(3), 034404 (2019).
48. Y. Y. Hui, X. Liu, W. Jie, *et al.*, "Exceptional tunability of band energy in a compressively strained trilayer MoS_2 sheet," ACS Nano **7**(8), 7126–7131 (2013).
49. H. J. Conley, B. Wang, J. I. Ziegler, *et al.*, "Bandgap engineering of strained monolayer and bilayer MoS_2," Nano Lett. **13**(8), 3626–3630 (2013).
50. M. W. Iqbal, K. Shahzad, R. Akbar, *et al.*, "A review on Raman finger prints of doping and strain effect in TMDCs," Microelectron. Eng. **219**, 111152 (2020).
51. B. Rajeswaran, R. Konar, R. Yitzhari, *et al.*, "Enhancement of the and Raman modes and layer identification of 2H-WS_2 nanosheets with metal coatings," J. Raman Spectrosc. **54**(9), 1030–1037 (2023).